

Special Collection

# Enhanced Pomegranate-Structured SnO<sub>2</sub> Electrocatalysts for the Electrochemical CO<sub>2</sub> Reduction to Formate

Kevin Van Daele,<sup>[a, b]</sup> Daniel Arenas-Esteban,<sup>[c]</sup> Daniel Choukroun,<sup>[a]</sup> Saskia Hoekx,<sup>[a, c]</sup> Alana Rossen,<sup>[a]</sup> Nick Daems,<sup>[a]</sup> Deepak Pant,<sup>[b, d]</sup> Sara Bals,<sup>[c]</sup> and Tom Breugelmans\*<sup>[a, d]</sup>

Although most state-of-the-art Sn-based electrocatalysts yield promising results in terms of selectivity and catalyst activity, their stability remains insufficient to date. Here, we demonstrate the successful application of the recently developed pomegranate-structured SnO<sub>2</sub> (Pom. SnO<sub>2</sub>) and SnO<sub>2</sub>@C (Pom. SnO<sub>2</sub>@C) nanocomposite electrocatalysts for the efficient electrochemical conversion of CO<sub>2</sub> to formate. With an initial selectivity of 83 and 86% towards formate and an operating potential of −0.72 V and −0.64 V vs. RHE, respectively, these pomegranate SnO<sub>2</sub> electrocatalysts are able to compete with most of the current state-of-the-art Sn-based electrocatalysts in terms of activity and selectivity. Given the importance of electrocatalyst stability, long-term experiments (24 h) were performed and a

temporary loss in selectivity for the Pom. SnO<sub>2</sub>@C electrocatalyst was largely restored to its initial selectivity upon drying and exposure to air. Of all the used (24 h) electrocatalysts, the pomegranate SnO<sub>2</sub>@C had the highest selectivity over a time period of one hour, reaching an average recovered Faradaic efficiency (FE) of 85%, while the commercial SnO<sub>2</sub> and bare pomegranate SnO<sub>2</sub> electrocatalysts reached an average of 79 and 80% FE towards formate, respectively. Furthermore, the pomegranate structure of Pom. SnO<sub>2</sub>@C was largely preserved due to the presence of the heterogeneous carbon shell, which acts as a protective layer, physically inhibiting particle segregation/pulverisation and agglomeration.

## Introduction

While anthropogenic CO<sub>2</sub> emissions continue to rise, bringing about disrupted weather patterns, acidification of the oceans, and an increased global average temperature, the price of renewable energy has fallen sharply over the past few decades, increasing the demand for intermittent renewable electricity storage.<sup>[1,2]</sup> A common solution to both problems could be found in the electrochemical CO<sub>2</sub> reduction (eCO<sub>2</sub>R) towards value-added products such as carbon monoxide (CO), ethylene

(C<sub>2</sub>H<sub>4</sub>), formic acid (FA, HCOOH), or methanol (CH<sub>3</sub>OH).<sup>[3,4]</sup> Careful selection of the electrocatalytic cathode material and reaction conditions enable the selective conversion of CO<sub>2</sub> towards a desired product.<sup>[4]</sup> Even though both carbon monoxide and formic acid involve a two-electron transfer, based on several techno-economical assessments, FA has the possibility to generate the highest revenue.<sup>[5,6]</sup> At present, FA is predominantly used in food chemicals, pharmaceuticals, and textiles, due to its strong reducing properties and acidic nature.<sup>[6]</sup> In the near future, however, FA could be utilized as a liquid hydrogen carrier or directly used in a direct formic acid fuel cell (DFAFC).<sup>[7,8]</sup>


Significant amounts of research have already been dedicated to making the electrochemical CO<sub>2</sub> reduction towards formic acid a viable option for converting anthropogenic CO<sub>2</sub> emissions and storing renewable electricity.<sup>[9]</sup> To this extent, numerous state-of-the-art Sn- and Bi-based electrocatalysts have been developed, yielding promising results in terms of selectivity, reaching > 90% Faradaic efficiency (FE%), an electrolyzer current density > 200 mA cm<sup>−2</sup>, and a catalyst activity > 50 A g<sup>−1</sup>.<sup>[10–13]</sup> Although Bi-based catalysts currently outperform Sn-based electrocatalysts in terms of stability and activity, Sn-based catalysts are still believed to be viable alternatives if an extended stability of over 80,000 hours can be achieved.<sup>[12,14]</sup> While both Bi and Sn are considered scarce materials, the estimated ultimately available resources for both metals are 20 and 300 Mt, respectively, making Sn more abundant than Bi.<sup>[15]</sup> Due to their high selectivity (FE%), low toxicity, non-noble nature, ecological and inexpensive properties, Sn-based electrocatalysts are an interesting candidate for the eCO<sub>2</sub>R towards FA.<sup>[10]</sup>


[a] K. V. Daele, D. Choukroun, S. Hoekx, A. Rossen, Dr. N. Daems, Prof. Dr. T. Breugelmans  
Applied Electrochemistry & Catalysis (ELCAT)  
University of Antwerp  
Universiteitsplein 1, 2610 Wilrijk (Belgium)  
E-mail: tom.breugelmans@uantwerpen.be  
Homepage: <https://elcat.be/tom-cv/>

[b] K. V. Daele, Dr. D. Pant  
Separation & Conversion Technology  
Flemish Institute for Technological Research (VITO)  
Boeretang 200, 2400 Mol (Belgium)

[c] Dr. D. Arenas-Esteban, S. Hoekx, Prof. Dr. S. Bals  
Electron Microscopy for Materials research (EMAT)  
University of Antwerp  
Groenenborgerlaan 171, 2020 Antwerp (Belgium)

[d] Dr. D. Pant, Prof. Dr. T. Breugelmans  
Center for Advanced Process Technology for  
Urban Resource Recovery (CAPTURE)  
Frieda Saeysstraat 1, 9052 Zwijnaarde (Belgium)

 Supporting information for this article is available on the WWW under <https://doi.org/10.1002/celec.202201024>

 An invited contribution to the *Plamen Atanassov Festschrift*

© 2023 The Authors. ChemElectroChem published by Wiley-VCH GmbH. This is an open access article under the terms of the Creative Commons Attribution License, which permits use, distribution and reproduction in any medium, provided the original work is properly cited.

*In situ* SnO<sub>2</sub> reduction, poisoning, particle detachment, dissolution, pulverisation, reshaping, or agglomeration are some of the major degradation pathways for Sn-based electrocatalysts, preventing long-term stability. Unfortunately, most of the aforementioned degradation mechanisms are irreversible, the only exceptions being *in situ* SnO<sub>2</sub> reduction and poisoning. Therefore, several mitigation strategies to prevent or decrease electrocatalyst degradation are becoming even more important.<sup>[16,17]</sup> In literature, promising results have been achieved using a particle confinement strategy.<sup>[18,19]</sup> Recently, the strategic use of a thin carbon shell which encapsulates the electrocatalytic nanoparticle has been highlighted by Yoo et al.<sup>[20,21]</sup> Acting as a protective layer, the thin carbon shell physically inhibits agglomeration and has also been demonstrated to prevent surface oxidation.

In this work, pomegranate-structured SnO<sub>2</sub> (Pom. SnO<sub>2</sub>) and -SnO<sub>2</sub>@Carbon (Pom. SnO<sub>2</sub>@C) electrocatalysts were synthesised and tested for the electrochemical CO<sub>2</sub> reduction towards formate. Prior to this work, Wen et al.<sup>[22]</sup> used these pomegranate SnO<sub>2</sub> and pomegranate SnO<sub>2</sub>@C nanocomposites, combined with Cu particles, as anodes for lithium-ion batteries. Due to their increased surface area, compared to commercial SnO<sub>2</sub> nanoparticles, and the possibility to synthesise them with and without an encapsulating carbon shell, we deemed them interesting electrocatalysts for the eCO<sub>2</sub>RR towards formate. These Pom. SnO<sub>2</sub> and Pom. SnO<sub>2</sub>@C electrocatalysts displayed an initial selectivity of 83 and 86% towards formate at an operating potential of -0.72 V and -0.64 V vs. RHE, respectively. Long-term experiments (24 h) revealed a largely preserved pomegranate structure for the carbon covered Pom. SnO<sub>2</sub>@C electrocatalyst, compared to the bare Pom. SnO<sub>2</sub>. Nonetheless, a temporary loss in selectivity for the Pom. SnO<sub>2</sub>@C electrocatalyst was observed. Upon drying and exposure to air, the initial selectivity was largely restored, and the pomegranate SnO<sub>2</sub>@C had the highest selectivity over a time period of one hour, reaching an average recovered FE of 85%, while the commercial SnO<sub>2</sub> and bare pomegranate SnO<sub>2</sub> electrocatalysts reached an average of 79 and 80% FE towards formate, respectively. We successfully demonstrated the use of a carbon shell to reduce the irreversible morphological electrocatalyst degradation and are able to largely restore the temporary selectivity loss for the Pom. SnO<sub>2</sub>@C electrocatalyst. Hereby, we confirmed and thoroughly investigated the unprecedented positive effect of an encapsulating carbon shell on the morphological stability of pomegranate-structured Sn-based electrocatalysts, yielding a promising mitigation strategy to enhance future electrocatalyst stability.

## Results and Discussion

### Physicochemical characterization

The particle morphology and size distribution of the commercial SnO<sub>2</sub> nanoparticles, pomegranate-structured SnO<sub>2</sub> and -SnO<sub>2</sub>@C electrocatalysts, prior to the electrochemical CO<sub>2</sub> reduction, were investigated by means of scanning electron

microscopy (SEM). As shown in Figure S1, the commercially available tin(IV) oxide nanopowder has a broad size distribution ( $\leq 100$  nm avg. part. size) and consists of smooth surfaced nanoparticles with varying morphology. Meanwhile, as shown in Figure S2, the synthesised pomegranate-structured SnO<sub>2</sub> electrocatalysts are spherical particles with a rough morphology (composed of even smaller nanoparticles) with a particle size of approximately 80 nm or smaller. Simultaneously, the pomegranate SnO<sub>2</sub>@C (Figure S3) nanocomposites appear to be smooth spheres due to the surrounding carbon shell. Furthermore, the particle size distribution of the pomegranate SnO<sub>2</sub>@C nanoparticles is similar to the pomegranate SnO<sub>2</sub> electrocatalyst, which is as expected, since both originate from the same batch.

Additional information concerning the crystalline structure, chemical nature, and space group symmetry of the commercial SnO<sub>2</sub>, pomegranate SnO<sub>2</sub>, and pomegranate SnO<sub>2</sub>@C electrocatalysts was obtained by X-ray powder diffraction (XRD). The diffractogram (Figure S4) displays the typical diffraction pattern with peaks at  $2\theta = 26.5^\circ, 33.8^\circ, 37.9^\circ, 38.9^\circ, 42.6^\circ, 51.7^\circ, 54.7^\circ, 57.7^\circ, 61.8^\circ, 64.6^\circ, 65.8^\circ, 71.1^\circ$  and  $78.5^\circ$ , present in a) commercial SnO<sub>2</sub> nanoparticles and nearly all present in b) pomegranate SnO<sub>2</sub> and c) pomegranate SnO<sub>2</sub>@C. These peaks are attributed to reflections of the (110), (101), (200), (111), (120), (211), (220), (002), (130), (112), (301), (202) and (321) planes, respectively, of tetragonal SnO<sub>2</sub> (COD #1534785).<sup>[23,24]</sup>

In literature currently no definitive consensus has been reached concerning the active site and selective species for the eCO<sub>2</sub>RR towards formate on Sn-based electrocatalysts.<sup>[25–28]</sup> Nevertheless, the importance of Sn oxide species, present in our pomegranate-structured electrocatalysts, has been highlighted for the selective eCO<sub>2</sub>RR towards formate.<sup>[29–35]</sup> For example, density functional theory (DFT) calculations by An et al.<sup>[36]</sup> found that a suitable ratio of Sn<sup>0</sup>/Sn<sup>2+</sup>/Sn<sup>4+</sup> results in a synergistic effect. The presence of tetravalent (Sn<sup>4+</sup>) and divalent (Sn<sup>2+</sup>) tin were shown to reduce the overpotential and improve formate selectivity, respectively, while the presence of Sn oxides/metal Sn interfaces aids in suppressing the competing hydrogen evolution reaction (HER).<sup>[36]</sup> While starting from a SnO<sub>2</sub>/Sn heterostructure might energetically favour formate production and suppress the HER, SnO<sub>2</sub> electrocatalysts have been demonstrated to be of a dynamic nature, enabling partial *in situ* reduction towards this presumably preferred SnO<sub>2</sub>/Sn Mott–Schottky heterojunction species, which makes for a more straightforward synthesis and warrants our choice of SnO<sub>2</sub> as a starting point.<sup>[37]</sup>

Insight into the possible electrochemically active surface area of all electrocatalysts was achieved by performing nitrogen (N<sub>2</sub>) physisorption and using the Brunauer-Emmett-Teller (BET) equation to calculate the specific surface area. The nitrogen adsorption-desorption isotherms of all samples (Figure S5) display a type IV isotherm with H3 hysteresis, according to the IUPAC classification of physisorption isotherms.<sup>[38]</sup> With a BET surface area of  $\approx 20$  m<sup>2</sup> g<sup>-1</sup>, the commercial SnO<sub>2</sub> nanoparticles have, ostensibly, the lowest amount of available active sites for the eCO<sub>2</sub>RR. The previously reported surface roughness of the pomegranate SnO<sub>2</sub> nanoparticles and the heterogeneous carbon shell of the pomegranate SnO<sub>2</sub>@C electrocatalyst offer a

larger surface area of  $\approx 47 \text{ m}^2 \text{ g}^{-1}$  and  $\approx 180 \text{ m}^2 \text{ g}^{-1}$ , respectively, which in theory should provide more active sites for the electrochemical conversion of  $\text{CO}_2$ .

Next, an indication concerning the electrochemically active surface area (ECSA) is derived from the electrochemical double layer capacitance ( $C_{\text{dl}}$ ) of the catalytic surface (Figure S6). The higher  $C_{\text{dl}}$  of the Pom.  $\text{SnO}_2$  (6.84 mF) electrocatalyst than that of the commercial  $\text{SnO}_2$  nanoparticles (3.48 mF) indicates a larger ECSA for the Pom.  $\text{SnO}_2$ , compared to the commercial  $\text{SnO}_2$  nanoparticles. Contrary to what was expected based on the BET surface areas, Pom.  $\text{SnO}_2$ @C yielded the lowest  $C_{\text{dl}}$  of 2.22 mF. Nevertheless, upon converting the  $C_{\text{dl}}$  to ECSA (i.e., by dividing the  $C_{\text{dl}}$  by the specific capacitance), a higher ECSA is expected for Pom.  $\text{SnO}_2$ @C as compared to the Pom.  $\text{SnO}_2$  and commercial  $\text{SnO}_2$  electrocatalysts, when looking at the specific capacitance for  $\text{SnO}_2$  ( $40\text{--}60 \mu\text{F cm}^{-2}_{\text{catalyst}}$ ) and carbon (approx.  $10 \mu\text{F cm}^{-2}_{\text{catalyst}}$ ) and considering the higher contribution of this carbon than the pomegranate structured  $\text{SnO}_2$  to the ECSA measurement of the Pom.  $\text{SnO}_2$ @C electrocatalyst.<sup>[39]</sup>

### Electrochemical $\text{CO}_2$ reduction

Electrocatalyst selectivity for the  $\text{eCO}_2\text{RR}$  towards formate was first investigated in a small ( $1 \text{ cm}^2$ ) flow-by electrolyzer by performing a 1 h chronopotentiometric experiment at a constant current density of  $100 \text{ mA cm}^{-2}$ . Figure 1 shows the operating potentials (V vs. RHE) and FE% towards formate plotted as a function of time for the commercial  $\text{SnO}_2$  nanoparticle- ( $\text{SnO}_2$ ), pomegranate  $\text{SnO}_2$ - (Pom.  $\text{SnO}_2$ ), and pomegranate  $\text{SnO}_2$ @C (Pom.  $\text{SnO}_2$ @C) electrocatalysts. With an average potential of  $-0.55 \text{ V}$  vs. RHE, the commercial  $\text{SnO}_2$  nanoparticles display an average selectivity (FE%) towards formate of 79%. A slightly more negative potential of  $-0.72 \text{ V}$  vs. RHE could be observed for the pomegranate  $\text{SnO}_2$ , which exhibit an excellent FE% of 83%. Finally, the pomegranate  $\text{SnO}_2$ @C nanocomposites display the highest selectivity for the  $\text{eCO}_2\text{RR}$  towards formate, i.e., 86%, and an operating potential between the other two samples, i.e.,  $-0.64 \text{ V}$  vs. RHE. In terms of selectivity and activity, both the commercial  $\text{SnO}_2$  nanoparticle electrocatalyst and pomegranate-structured  $\text{SnO}_2$  and  $\text{SnO}_2$ @C nanocomposite electrocatalysts belong amongst the

best Sn-based materials reported thus far for the  $\text{eCO}_2\text{RR}$  towards FA (Table S1).<sup>[10,11,16]</sup>

For the  $\text{eCO}_2\text{RR}$  towards formic acid to become industrially relevant, prolonged electrocatalyst stability should be attained.<sup>[12,14]</sup> Initial insights concerning the stability of the  $\text{SnO}_2$ , Pom.  $\text{SnO}_2$  and Pom.  $\text{SnO}_2$ @C electrocatalysts were obtained by performing 24 h chronopotentiometric measurements ( $100 \text{ mA cm}^{-2}$ ), combined with post-electrolysis *ex situ* transmission electron microscopy (TEM). Figure 2 displays the average operating potential and FE% towards formate plotted as function of time. Here, it is noticed that while the operating potential remains relatively stable at  $-0.49 \text{ V}$  and  $-0.62 \text{ V}$  vs. RHE for the commercial  $\text{SnO}_2$  and pomegranate  $\text{SnO}_2$  electrocatalysts, respectively, the operating potential of the pomegranate  $\text{SnO}_2$ @C electrocatalyst continues to become more negative, decreasing from  $-0.64 \text{ V}$  to  $-0.88 \text{ V}$  vs. RHE, over the course of the 24 h experiment.

Interestingly, the FE% towards formate of both the commercial  $\text{SnO}_2$  and pomegranate  $\text{SnO}_2$  are relatively stable at an average of 81% and 83%, respectively, while the FE% of the pomegranate  $\text{SnO}_2$ @C nanocomposites experiences a decrease from 83% (after 15 minutes) to 46% (after 24 hours). These results appear to counter the hypothesis that the carbon shell would increase the electrocatalyst stability, by acting as a protective layer, physically inhibiting particle agglomeration.

After these long-term experiments, the used gas diffusion electrodes (GDEs) were left to dry under air (with no washing involved) and the electrochemical performance of the used electrocatalysts was evaluated again. Figure 3 shows the comparison in average FE% towards formate, for a 1-hour electrolysis at  $100 \text{ mA cm}^{-2}$ , between a newly spray coated and used GDE. For all samples the selectivity of the GDE that had previously been used for 24 h is slightly lower, yet comparable to the initial (new) FE%. The loss of selectivity for the Pom.  $\text{SnO}_2$ @C electrocatalyst could thus, for the most part, be restored to its original FE% by leaving the electrode to dry under air. Of all the used (24 h) electrocatalysts, the pomegranate  $\text{SnO}_2$ @C had the highest selectivity over a time period of one hour, reaching an average recovered FE% of 85%, while the commercial  $\text{SnO}_2$  and pomegranate  $\text{SnO}_2$  electrocatalysts reached an average of 79 and 80% FE% towards formate, respectively.

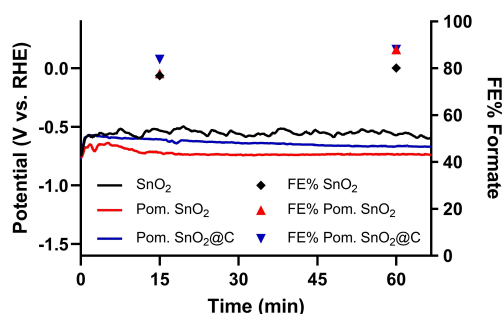


**Figure 1.** Average IR-compensated potential (V vs. RHE) and FE% towards formate plotted as function of time (min) at a constant current density of  $100 \text{ mA cm}^{-2}$  for 1 h.

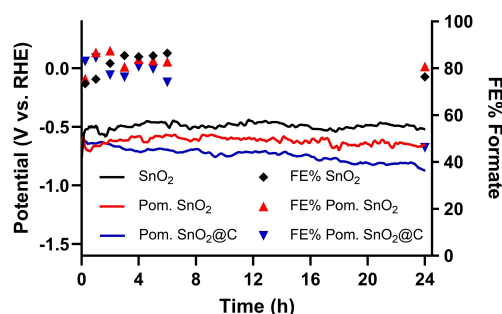


**Figure 2.** Average IR-compensated potential (V vs. RHE) and FE% towards formate plotted as function of time (min) at a constant current density of  $100 \text{ mA cm}^{-2}$  for 24 h.

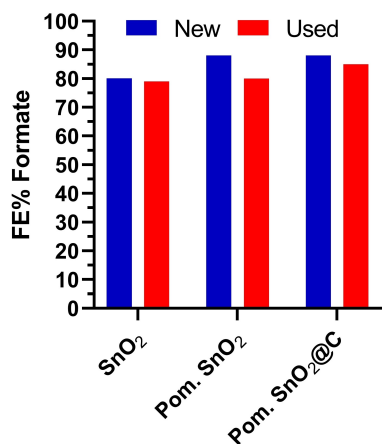


**Figure 3.** Average Faradaic efficiency towards formate, over a 1 h electrolysis at 100 mA cm<sup>-2</sup>, of a new (blue) and used (red) GDE, spray coated with a commercial SnO<sub>2</sub> nanoparticle (SnO<sub>2</sub>), Pomegranate SnO<sub>2</sub> (Pom. SnO<sub>2</sub>) or Pomegranate SnO<sub>2</sub>@C (Pom. SnO<sub>2</sub>@C) electrocatalyst.

To elucidate the loss and recovery of the selectivity of the Pom. SnO<sub>2</sub>@C electrocatalyst, *ex situ* high angle annular dark-field scanning transmission electron microscopy (HAADF-STEM) imaging and energy dispersive X-ray spectroscopy (EDS) mapping were used to investigate the pomegranate SnO<sub>2</sub> (Figure 4) and pomegranate SnO<sub>2</sub>@C (Figure 5) electrocatalysts, before and after 24 h electrolysis. For the Pom. SnO<sub>2</sub> electrocatalyst, low-magnification HAADF-STEM images, acquired before (Figure 4a) and after (Figure 4d) electrolysis, show a clear

agglomeration of nanoparticles as well as a loss of the characteristic pomegranate shape after 24 h of electrolysis. At higher magnification, HAADF-STEM and fast Fourier transformations (FFT) (Figure 4b) show that the pomegranate SnO<sub>2</sub> nanostructures, prior to electrolysis, are composed of smaller, randomly oriented, crystalline SnO<sub>2</sub> nanoparticles, as previously indicated by the XRD diffractogram. Furthermore, EDS mapping confirms the presence of Sn and O on both Pom. SnO<sub>2</sub> samples, prior to (Figure 4c) and after (Figure 4f) 24 h electrochemical CO<sub>2</sub> reduction and drying in air. Even though the FE% towards formate remains relatively stable, clear nanoparticle segregation/pulverization and agglomeration could be observed in Figure 4e in comparison to Figure 4a. These phenomena have previously been reported by He et al. and Wu et al.,<sup>[40,41]</sup> where this change in the particles' physicochemical properties always resulted in a loss of FE%. Here, no significant loss of selectivity was observed after 24 h. Nonetheless, the effects of this irreversible morphological degradation may start to appear in the FE% in the long run (> 24 h). Therefore, further investigation is necessary to unravel the effect of these morphological changes on the long-term stability and selectivity of the pomegranate SnO<sub>2</sub> electrocatalyst. Accelerated degradation tests combined with *ex situ* characterisation are a promising method for efficient and rapid investigation.<sup>[16]</sup>

In the case of the Pom. SnO<sub>2</sub>@C electrocatalyst, low magnification HAADF-STEM images and EDS maps before (Figure 5a) and after (Figure 5d) electrolysis show similar pomegranate structures, indicating that the heterogeneous layer of carbon covering the particles seems to successfully

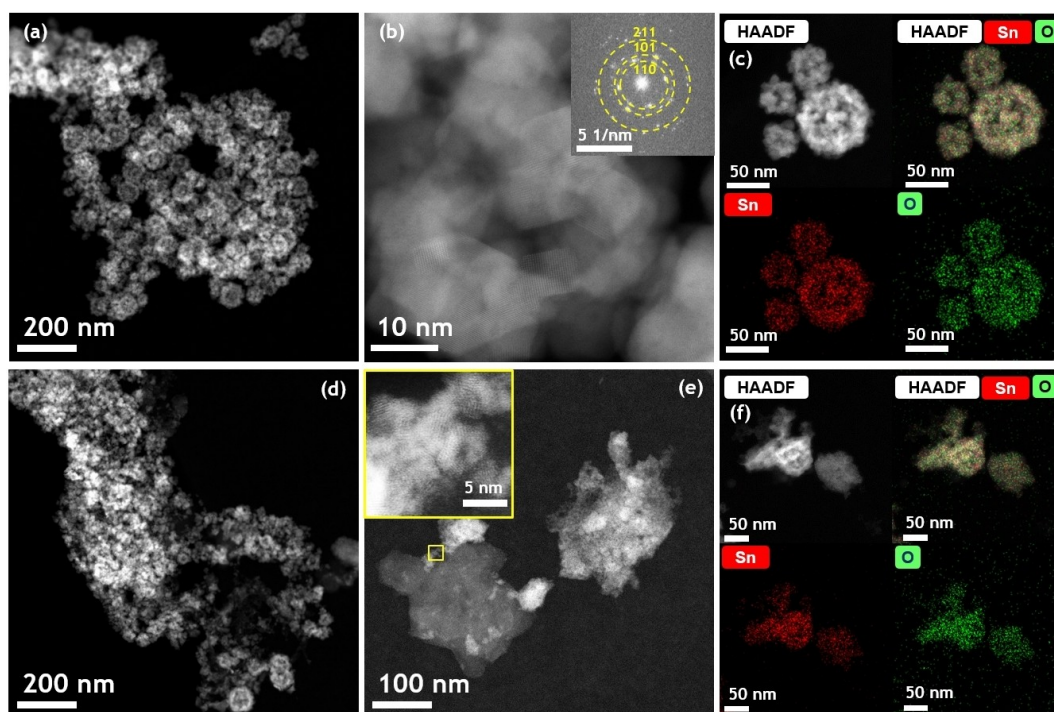


**Figure 4.** HAADF-STEM image of pomegranate SnO<sub>2</sub> nanoparticles before (a) and after (d) electrochemical CO<sub>2</sub> reduction. High-resolution HAADF-STEM image from which it can be verified that the pomegranate nanostructures are formed by SnO<sub>2</sub> nanoparticles, which is further confirmed by the crystalline structure observed in the FFT (b). HAADF-STEM image of the segregation and agglomeration of small SnO<sub>2</sub> nanoparticles after current application (e), and HAADF-STEM images and EDS maps of the nanoparticles before (c) and after (f) the electrochemical experiment. EDS confirms the presence of Sn and O on both samples.



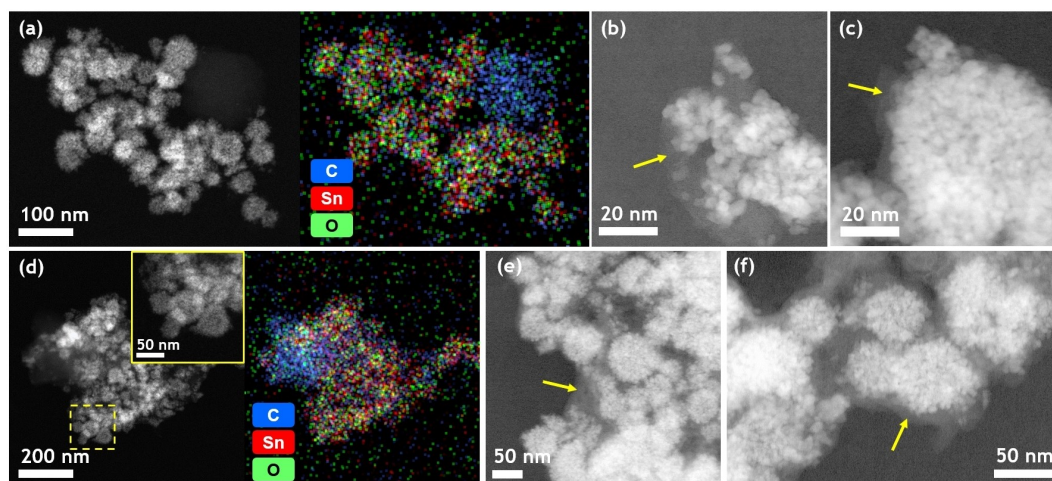


**Figure 5.** HAADF-STEM image and EDS map of the pomegranate  $\text{SnO}_2@C$  particles before (a) and after (d) electrochemical  $\text{CO}_2$  reduction where similar particle morphology is observed (inset of magnified area marked in yellow), indicating that the carbon shell helps to better retain the original morphology. EDS maps show a heterogeneous distribution of carbon over both samples. LAADF-STEM images of the sample before (b, c) and after (e, d) current application show the heterogeneous carbon coverage in light grey, as indicated by the yellow arrows, over the pomegranate  $\text{SnO}_2$  particles.

prevent particle agglomeration/segregation. A careful selection of the acquisition semi-angle in dark field mode of the electron microscope was necessary for the correct visualization of the carbon layer because the high contrast from the  $\text{SnO}_2$  nanoparticles masks the carbon signal at high convergence semi-angles. Therefore, low angle annular dark-field scanning transmission electron microscopy (LAADF-STEM) mode was used to reveal the carbon coverage (in light grey, as indicated by the yellow arrows) over the pomegranate  $\text{SnO}_2$  particles before (Figure 5b and c) and after (Figure 5e and f) 24 h electrolysis, showing that it's quite heterogeneous and no complete carbon coverage was obtained. These results show that although a loss in porosity could not be entirely prevented, the heterogeneous carbon shell was able to moderately suppress particle agglomeration. Since even a partially covering heterogeneous carbon shell is able to, to a certain extent, protect the pomegranate  $\text{SnO}_2$  nanoparticles from irreversible morphological changes, further improvements to the electrocatalysts stability could be achieved by perfecting the synthesis procedure and achieving a fully covering, homogenous carbon shell. The temporary loss in selectivity over the course of a 24 h electrolysis, therefore, appears to be caused by a degradation pathway other than segregation and agglomeration.

Given these results, particle segregation/pulverisation and agglomeration are highly unlikely to be the cause of the observed temporary decrease in FE% for the Pom.  $\text{SnO}_2@C$  electrocatalyst. Other possible explanations could be the loss of GDE hydrophobicity, resulting in flooding and salt crystallization, *in situ*  $\text{SnO}_2$  reduction, or poisoning of the electrocatalyst.<sup>[16,17,42,43]</sup> While a small amount of perspiration was noticed during all 24 measurements, we found that this could not solely explain the temporary decrease of selectivity of the pomegranate  $\text{SnO}_2@C$  electrocatalyst. Furthermore, no excessive salt crystallization was observed and the electrocatalysts were able to largely recover their initial selectivity by

drying under air without any washing. Since electrocatalyst poisoning generally originates from reaction intermediates or impurities from the electrolyte, electrolyzer components, or  $\text{CO}_2$  feed,<sup>[44]</sup> we deemed it highly unlikely for this to exclusively occur with the Pom.  $\text{SnO}_2@C$  electrocatalyst. Nonetheless, the covering heterogeneous carbon shell may change the local environment of the electrocatalyst compared to the commercial  $\text{SnO}_2$  and Pom.  $\text{SnO}_2$  electrocatalyst, which could result in the possible trapping of reaction intermediates or other changes in the carbon shell of the Pom.  $\text{SnO}_2@C$ .<sup>[45]</sup> Given that the loss of selectivity was largely recovered by leaving the used Pom.  $\text{SnO}_2@C$  GDE to dry under air, *in situ* reduction of  $\text{SnO}_2$  to metallic  $\text{Sn}^0$  under the harsh cathodic operating conditions and subsequent re-oxidation in air appear to be the main cause of the temporary loss of selectivity.<sup>[28]</sup>

To confirm our hypothesis, additional *ex situ* physicochemical characterization for both electrocatalysts was performed on both pristine pray coated GDEs and used electrodes. Firstly, *ex situ* XRD (Figure 6), after 24 h of electrolysis, clearly indicates a change in the oxidation state of the pomegranate  $\text{SnO}_2$  nanocomposites when comparing the Pom.  $\text{SnO}_2$  and Pom.  $\text{SnO}_2@C$  diffractogram from before and after the  $\text{eCO}_2\text{RR}$ , respectively. It appears that upon electrolysis a reduction of the pristine  $\text{SnO}_2$  structure indeed occurs, as is evidenced by the appearance of peaks that can be ascribed to metallic Sn (COD #9008570).<sup>[46]</sup> Due to the large surface area ( $S_{\text{BET}}$ ) and strong carbon signal, originating from the GDE and Pom.  $\text{SnO}_2@C$  itself, a quantitative analysis isn't possible, and it thus remains unclear which sample underwent the most significant *in situ* reduction. Therefore, *ex situ* X-ray photoelectron spectroscopy (XPS) and a sputter depth profile were recorded on both electrodes after 24 h of electrolysis, until a stable Sn signal was obtained. Re-oxidation of both samples after electrolysis was minimized by storing and transferring all samples under an inert argon atmosphere. Figure 7 shows the high-resolution Sn  $3d_{5/2}$  XPS

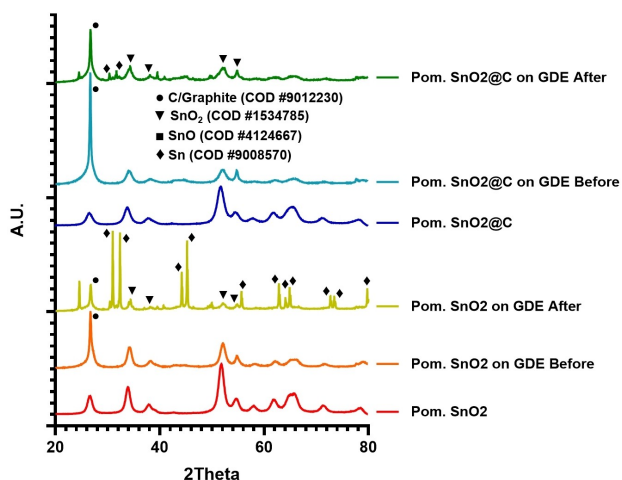


**Figure 6.** *Ex situ* XRD diffractogram of Pom. SnO<sub>2</sub> and Pom. SnO<sub>2</sub>@C before and after 24 h of eCO<sub>2</sub>RR, compared with the Crystallography Open Database (COD) #9012230 for graphite, #1534785 for SnO<sub>2</sub>, #4124667 for SnO and #9008570 for Sn.<sup>[23,24,46,48,49]</sup>

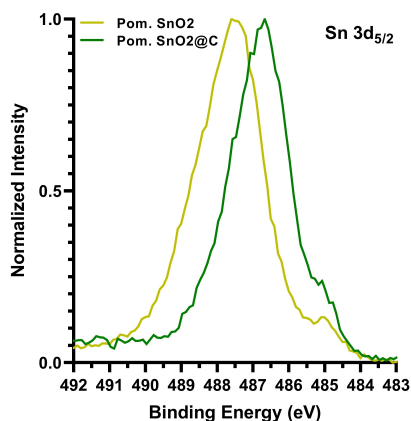


**Figure 7.** *Ex situ* high resolution Sn 3d<sub>5/2</sub> XPS spectra of Pom. SnO<sub>2</sub> and Pom. SnO<sub>2</sub>@C after 24 h of eCO<sub>2</sub>RR.<sup>[47]</sup>

spectrum for both samples after 24 h of electrolysis. Both Pom. SnO<sub>2</sub> and Pom. SnO<sub>2</sub>@C show a large 3d<sub>5/2</sub> peak with an asymmetry at lower binding energies, revealed as a small shoulder, indicating the presence of metallic Sn<sup>0</sup>. The final obtained high resolution Sn 3d XPS spectra were normalized and shifted to match the metallic Sn binding energy (485 ± 0.5 eV).<sup>[47]</sup> Comparing the higher binding energy contribution, a clear shift can be noticed which is presumably caused by different types of Sn bonds. More importantly, these results confirm that, after 24 h of eCO<sub>2</sub>RR, the Pom. SnO<sub>2</sub>@C electrocatalyst encompasses more reduced Sn<sup>0</sup>, compared to the Pom. SnO<sub>2</sub> without carbon shell, as evidenced by the increased intensity of the metallic Sn shoulder at a binding energy of 485 eV. This clearly indicates faster and more pronounced *in situ* SnO<sub>2</sub> reduction of the former, which isn't offset by the morphological electrocatalyst degradation revealing new and selective SnO<sub>x</sub> active sites, as suspected for the Pom. SnO<sub>2</sub>. Consequently, utilising *ex situ* XRD and XPS, we were able to

unambiguously link the temporary selectivity loss of the Pom. SnO<sub>2</sub>@C electrocatalyst to the *in situ* SnO<sub>2</sub> reduction to Sn<sup>0</sup>.

As described by Dutta et al.<sup>[30,31]</sup> the *in situ* reduction of SnO<sub>2</sub> is one of the few degradation pathways which seems to be partially reversible. While *in situ* SnO<sub>2</sub> reduction occurs in all samples, since their operating potentials are comparable, the segregation and agglomeration observed in the Pom. SnO<sub>2</sub> sample could offset and postpone the decrease in selectivity by providing new and selective Sn<sup>4+</sup> or Sn<sup>2+</sup> active sites, originating from the core of the original nanoparticles. Although the heterogeneously covering carbon shell largely ensures the preservation of the pomegranate-structured morphology, it also provides a higher conductivity and currently isn't fully covering the pomegranate-structured SnO<sub>2</sub> nanoparticles. Therefore, it probably causes a more rapid depletion of the selective Sn<sup>4+</sup> or Sn<sup>2+</sup> sites, ensuring a more rapid loss in selectivity, in comparison to the commercial SnO<sub>2</sub> and Pom. SnO<sub>2</sub> electrocatalysts. Improved synthesis of the Pom. SnO<sub>2</sub>@C electrocatalyst, ensuring a homogeneous and fully covering carbon shell has the potential to further increase its long-term electrocatalytic stability by inhibiting irreversible morphological changes and protecting the pomegranate SnO<sub>2</sub> nanocomposites against *in situ* reduction.

## Conclusion

In conclusion, we have successfully synthesised previously reported pomegranate-structured SnO<sub>2</sub> and SnO<sub>2</sub>@C nanocomposite electrocatalysts and demonstrated its use as a promising catalyst for the selective eCO<sub>2</sub>R to formate. With an initial selectivity of 83 and 86 % towards formate, for the Pom. SnO<sub>2</sub> and Pom. SnO<sub>2</sub>@C, respectively, these novel catalysts are able to compete with most current state-of-the-art Sn-based electrocatalysts in terms of activity and selectivity. Furthermore, the pomegranate SnO<sub>2</sub> electrocatalyst exhibits an excellent 24 h stability, maintaining an average FE% formate of 83 %. Counter-intuitively, the Pom. SnO<sub>2</sub>@C electrocatalyst, which retained its morphology much better, as confirmed by HAADF-STEM imaging, displayed a decrease in FE% towards formate from 83 % (after 15 minutes) to 46 % (after 24 hours). This loss of selectivity, however, proved to be temporary since we were able to restore most of its selectivity to its original FE% by leaving the electrode to dry in air. Out of all the used (24 h) electrocatalysts, the pomegranate SnO<sub>2</sub>@C had the highest selectivity over a time period of one hour, reaching an average recovered FE% of 85 %, while the commercial SnO<sub>2</sub> and pomegranate SnO<sub>2</sub> electrocatalysts reached an average of 79 and 80 % FE% towards formate, respectively. *Ex situ* XRD and XPS were used to link this temporary selectivity loss of the Pom. SnO<sub>2</sub>@C electrocatalyst to the *in situ* SnO<sub>2</sub> reduction to metallic Sn. While this electrochemical degradation occurs in both electrocatalysts, it is more pronounced in the Pom. SnO<sub>2</sub>@C electrocatalyst since it isn't offset by the morphological electrocatalyst degradation revealing new and selective SnO<sub>x</sub> active sites, as suspected for the Pom. SnO<sub>2</sub>. Finally, the use of a carbon shell was demonstrated to reduce the irreversible

morphological electrocatalyst degradation and we were able to largely restore the temporary selectivity loss for the Pom. SnO<sub>2</sub>@C electrocatalyst. Further research will be devoted to unravelling and increasing the stability of these novel pomegranate-structured electrocatalysts by perfecting their synthesis to obtain a pomegranate SnO<sub>2</sub>@C electrocatalyst with a homogeneous carbon shell and performing accelerated degradation tests to predict their long-term stability.

## Experimental Section

### Materials

The following chemicals and commercial electrocatalyst were used as received, without any further purification: d-glucose (anhydrous, biotechnology grade, VWR Life Science), D520 NAFION® solution (Ion Power), ethanol (99.8%, abs. p., Chem-Lab), potassium hydrogen carbonate (99.5 + %, v.p., Chem-Lab), potassium hydroxide (85 + %, pellets a.r., Chem-Lab), propanol-2 (99.8 + %, iso-propanol a.r., Chem-Lab), sodium tin(IV) oxide trihydrate (98%, Alfa Aesar), tin(IV) oxide (nanopowder, ≤ 100 nm avg. part. size, Sigma-Aldrich).

### Synthesis of the pomegranate SnO<sub>2</sub> and SnO<sub>2</sub>@C nanoparticles

Pomegranate-structured SnO<sub>2</sub> and SnO<sub>2</sub>@C nanoparticles were prepared via a method adapted from Wen *et al.*,<sup>[22]</sup> by dissolving 20 mmol sodium stannate (Na<sub>2</sub>SnO<sub>3</sub>·3H<sub>2</sub>O) in 100 mL of a 1 M aqueous glucose solution. After 1 hour of sonication the solution was transferred into two teflon-lined stainless steel autoclaves and placed in an oven at 180 °C. After 4 hours, the autoclaves were rapidly cooled down to room temperature and the precipitates were collected via centrifugation. Subsequently, the obtained precipitates were washed three times with deionized water and ethanol. After drying overnight at 100 °C, pomegranate-structured SnO<sub>2</sub> and SnO<sub>2</sub>@C nanoparticles were acquired through a final heat treatment at 550 °C (2 °C min<sup>-1</sup>) for 4 h under air and argon atmosphere respectively.

### Physicochemical characterization

Nitrogen (N<sub>2</sub>) physisorption was performed at 77 K with a Quantachrome Quadrasorb SI (Quantachrome Instruments, Boynton Beach, FL, USA) automated surface area & pore size analyzer. Prior to the measurements, all samples were degassed for 16 h at 200 °C. The specific surface area was calculated using the Brunauer-Emmet-Teller (BET) equation.

XRD was measured on a Bruker D8 ECO powder diffractometer with a LYNXEYE XE-T detector and Cu K-Alpha radiation. All samples were probed from 0–80° or 20–80° 2θ and compared with the crystallography open database (COD) #1534785 for tetragonal SnO<sub>2</sub>, #9012230 for graphite, #4124667 for SnO and #9008570 for Sn.

SEM measurements were carried out using a ThermoFisher Scientific Quanta FEG 250 equipped with an ETD detector, operated at an acceleration voltage of 10 and 20 kV.

HAADF-STEM and LAADF-STEM as well as EDS were performed using an aberration-corrected cubed Thermo Fisher Scientific Titan microscope operating at 300 kV and equipped with a Super X EDS detector. EDS analysis was performed by acquiring at least 200 frames at a higher current of 150 pA to ensure sufficient signal.

HAADF-STEM was realized using a collection angle between 46 to 215 mrad, while LAADF-STEM was realized using a collection angle between 19 to 74 mrad, to be able to visualize the carbon shell near the SnO<sub>2</sub> nanoparticles. EDS experiments for pomegranate SnO<sub>2</sub>@C samples were performed using Si<sub>3</sub>N<sub>4</sub> grids to be able to correctly map the carbon signal in the sample.

XPS was performed on a PHI-VersaProbe III, using an Al Kα (1486.6 eV) monochromatic X-ray source. An area of Ø 100 μm was measured, using a pass energy of 26 eV for the high resolution (HR) spectra and an automatic neutraliser. The PHI MultiPak software was used for processing the Sn 3d XPS spectra.

### Electrochemically active surface area and uncompensated resistance determination

The ECSA was derived from the electrochemical double layer capacitance (C<sub>dl</sub>) of the catalytic surface, measured on pristine electrocatalyst coated gas diffusion electrodes, prior to the electrochemical CO<sub>2</sub> reduction. Multiple cyclic voltammetry experiments were performed, in a non-faradaic region, at scan rates of 80, 120, 160, 200, 240, 280 and 320 mV s<sup>-1</sup>. A linear regression was plotted between the capacitive current density differences in the middle of the potential window and the scan rate.

The uncompensated resistance R<sub>u</sub> (Ohmic drop) was determined prior to all electrochemical CO<sub>2</sub> reduction experiments, by means of a current interrupt measurement. To his extent, a constant potential of -4 V vs. Ag/AgCl was applied before triggering the current interrupt circuit and measuring the potential decay over a time period of 2 ms. The uncompensated resistance is then obtained from a linear regression between 0 s and 500 μs in the Metrohm Autolab Nova 2.1.5 Software for electrochemical research. All potentials were corrected for this resistance.

### Electrochemical CO<sub>2</sub> reduction

Commercial SnO<sub>2</sub> nanoparticles and the as-synthesised pomegranate-structured SnO<sub>2</sub> and SnO<sub>2</sub>@C electrodes were prepared by spray coating a Sigracet 39 BB gas diffusion electrode (GDE) with an ink made from the obtained electrocatalyst powders. For each deposition, 75 mg of the electrocatalyst powder is dispersed with 0.3750 g of a 5 wt% Nafion solution in approximately 10 mL of a 1:1 Milli-Q (18.2 MΩ·cm @ 25 °C):IPA Solution. A GDE of 25 cm<sup>2</sup> is slowly and uniformly spray coated before being divided into 6 smaller GDEs with a projected area of approximately 3 cm<sup>2</sup> and the targeted electrocatalyst loading of 1.5 mg cm<sup>-2</sup>. These spray coated GDEs are then used as cathodes in a small-flow by electrolyzer with a geometric electrochemically active surface area of 1 cm<sup>2</sup>.

Chronopotentiometric experiments of 1 hour were conducted in the abovementioned flow-by electrolyzer at an applied current density of -100 mA cm<sup>-2</sup>. The catholyte, 0.5 M KHCO<sub>3</sub>, was pumped single pass at a flow rate of 2 mL min<sup>-1</sup>, while the anolyte, 2 M KOH, was recycled at an equal flow rate over a Ni foam anode. Furthermore, a Nafion 117 membrane and Ag/AgCl reference electrode were used. Liquid samples were taken after 15 minutes and after 1 hour to determine the FE% towards formate by means of HPLC. Long-term 24 h chronopotentiometric experiments were conducted under identical circumstances, where the FE% towards formate was determined after 15 minutes and every hour for the first 6 hours and once again after 24 h. The reported data was reproduced, and an average value is reported for all FE% and IR-compensated potentials.



## Acknowledgements

K. Van Daele was financially supported through a PhD fellowship strategic basic research (1S83320N) from the Research Foundation Flanders (FWO). Furthermore, this work was supported by the Interreg 2 Seas-program 2014–2020, co-funded by the European Regional Development Fund under subsidy contract No E2C 2S03-019 (UA & VITO). This project also received funding in the framework of the Catalisti cluster SBO project CO2PERATE (“All renewable CCU based on formic acid integrated in an industrial micro-grid”), with financial support of VLAIO (Flemish Agency for Innovation and Entrepreneurship) (UA & VITO). Additionally, we acknowledge Prof. Tom Hauffman and Kitty Baert from the Electrochemical and Surface Engineering research group (SURF) at the VUB (Vrije Universiteit Brussel) for the X-ray Photoelectron Spectroscopy measurements. Finally, the authors recognize the contribution of LADCA (Laboratory of Adsorption and Catalysis) and iPRACS (Intelligence in Processes, Advanced Catalysts and Solvents), both research groups at the University of Antwerp, for the nitrogen physisorption and X-ray powder diffraction measurements, respectively.

## Conflict of Interest

There are no conflicts of interest to declare.

## Data Availability Statement

The data that support the findings of this study are available from the corresponding author upon reasonable request.

**Keywords:** electrochemical CO<sub>2</sub> reduction · formate · metal-oxide/carbon interfaces · porous nanoparticles · SnO<sub>2</sub>

- [1] B. Obama, *Science* **2017**, *355*, 126–129.
- [2] Y. Y. Birdja, E. Pérez-Gallent, M. C. Figueiredo, A. J. Göttle, F. Calle-Vallejo, M. T. M. Koper, *Nat. Energy* **2019**, *4*, 732–745.
- [3] R. G. Grim, Z. Huang, M. T. Guarnieri, J. R. Ferrell, L. Tao, J. A. Schaidle, *Energy Environ. Sci.* **2020**, *13*, 472–494.
- [4] O. S. Bushuyev, P. De Luna, C. T. Dinh, L. Tao, G. Saur, J. van de Lagemaat, S. O. Kelley, E. H. Sargent, *Joule* **2018**, *2*, 825–832.
- [5] C. Chen, J. F. Khosrowabadi Kotyk, S. W. Sheehan, *Chem* **2018**, *4*, 2571–2586.
- [6] M. Pérez-Fortes, J. C. Schöneberger, A. Boulamanti, G. Harrison, E. Tzimas, *Int. J. Hydrogen Energy* **2016**, *41*, 16444–16462.
- [7] H. Xiang, H. A. Miller, M. Bellini, H. Christensen, K. Scott, S. Rasul, E. H. Yu, *Sustain. Energy Fuels* **2020**, *4*, 277–284.
- [8] B. Thijs, J. Rongé, J. A. Martens, *Green Chem.* **2022**, *24*, 2287–2295.
- [9] S. A. Al-Tamreh, M. H. Ibrahim, M. H. El-Naas, J. Vaes, D. Pant, A. Benamor, A. Amhamed, *ChemElectroChem* **2021**, *8*, 3207–3220.
- [10] S. Zhao, S. Li, T. Guo, S. Zhang, J. Wang, Y. Wu, Y. Chen, *Nano-Micro Lett.* **2019**, *11*, 62.
- [11] Z. Yang, F. E. Oropeza, K. H. L. Zhang, *APL Mater.* **2020**, *8*, 060901.
- [12] R. I. Masel, Z. Liu, H. Yang, J. J. Kaczur, D. Carrillo, S. Ren, D. Salvatore, C. P. Berlinguette, *Nat. Nanotechnol.* **2021**, *16*, 118–128.
- [13] D. Xia, H. Yu, H. Xie, P. Huang, R. Menzel, M. M. Titirici, G. Chai, *Nanoscale* **2022**, *14*, 7957–7973.
- [14] M. G. Kibria, J. P. Edwards, C. M. Gabardo, C. T. Dinh, A. Seifitokaldani, D. Sinton, E. H. Sargent, *Adv. Mater.* **2019**, *31*, 1–24.
- [15] T. Henckens, *Resour. Conserv. Recycl.* **2021**, *169*, 105511.
- [16] K. Van Daele, B. De Mot, M. Pupo, N. Daems, D. Pant, R. Kortlever, T. Breugelmans, *ACS Energy Lett.* **2021**, *6*, 4317–4327.
- [17] S. Popović, M. Smiljanić, P. Jovanović, J. Vavra, R. Buonsanti, N. Hodnik, *Angew. Chem. Int. Ed.* **2020**, *59*, 14736–14746; *Angew. Chem.* **2020**, *132*, 14844–14854.
- [18] F. Lei, W. Liu, Y. Sun, J. Xu, K. Liu, L. Liang, T. Yao, B. Pan, S. Wei, Y. Xie, *Nat. Commun.* **2016**, *7*, 12697.
- [19] Y. E. Kim, W. Lee, M. H. Youn, S. K. Jeong, H. J. Kim, J. C. Park, K. T. Park, *J. Ind. Eng. Chem.* **2019**, *78*, 73–78.
- [20] L. Pacquets, J. Van Den Hoek, D. Arenas-Esteban, R. G. Ciocarlan, P. Cool, K. Baert, T. Hauffman, N. Daems, S. Bals, T. Breugelmans, *ACS Appl. Nano Mater.* **2022**, *5*, 7723–7732.
- [21] J. M. Yoo, H. Shin, D. Y. Chung, Y. E. Sung, *Acc. Chem. Res.* **2022**, *55*, 1278–1289.
- [22] W. Wen, M. Zou, Q. Feng, J. Li, L. Guan, H. Lai, Z. Huang, *Electrochim. Acta* **2015**, *182*, 272–279.
- [23] S. Graulis, D. Chateigner, R. T. Downs, A. F. T. Yokochi, M. Quirós, L. Lutterotti, E. Manakova, J. Butkus, P. Moeck, A. Le Bail, *J. Appl. Crystallogr.* **2009**, *42*, 726–729.
- [24] H. Seki, N. Ishizawa, N. Mizutani, M. Kato, *J. Ceram. Assoc. Japan* **1984**, *92*, 219–223.
- [25] C. Cui, H. Wang, X. Zhu, J. Han, Q. Ge, *Sci. China Chem.* **2015**, *58*, 607–613.
- [26] C. Cui, J. Han, X. Zhu, X. Liu, H. Wang, D. Mei, Q. Ge, *J. Catal.* **2016**, *343*, 257–265.
- [27] M. F. Baruch, J. E. Pander, J. L. White, A. B. Bocarsly, *ACS Catal.* **2015**, *5*, 3148–3156.
- [28] C. Salvini, M. Re Fiorentin, F. Risplendi, F. Raffone, G. Cicero, *J. Phys. Chem. C* **2022**, *126*, 14441–14447.
- [29] G. B. Damas, C. R. Miranda, R. Sgarbi, J. M. Portela, M. R. Camilo, F. H. B. Lima, C. M. Araujo, *Catalysts* **2019**, *9*, 636.
- [30] A. Dutta, A. Kuzume, M. Rahaman, S. Vesztergom, P. Broekmann, *ACS Catal.* **2015**, *5*, 7498–7502.
- [31] A. Dutta, A. Kuzume, V. Kaliginedi, M. Rahaman, I. Sinev, M. Ahmadi, B. Roldán Cuenya, S. Vesztergom, P. Broekmann, *Nano Energy* **2018**, *53*, 828–840.
- [32] R. Zhang, W. Lv, L. Lei, *Appl. Surf. Sci.* **2015**, *356*, 24–29.
- [33] Y. Chen, M. W. Kanan, *J. Am. Chem. Soc.* **2012**, *134*, 1986–1989.
- [34] S. Liu, F. Pang, Q. Zhang, R. Guo, Z. Wang, Y. Wang, W. Zhang, J. Ou, *Appl. Mater. Today* **2018**, *13*, 135–143.
- [35] X. Cao, B. Wulan, B. Zhang, D. Tan, J. Zhang, *J. Mater. Chem. A* **2021**, *9*, 14741–14751.
- [36] X. An, S. Li, A. Yoshida, Z. Wang, X. Hao, A. Abudula, G. Guan, *ACS Sustainable Chem. Eng.* **2019**, *7*, 9360–9368.
- [37] S. Ning, J. Wang, D. Xiang, S. Huang, W. Chen, S. Chen, X. Kang, *J. Catal.* **2021**, *399*, 67–74.
- [38] M. Thommes, K. Kaneko, A. V. Neimark, J. P. Olivier, F. Rodriguez-Reinoso, J. Rouquerol, K. S. W. Sing, *Pure Appl. Chem.* **2015**, *87*, 1051–1069.
- [39] C. Wei, S. Sun, D. Mandler, X. Wang, S. Z. Qiao, Z. J. Xu, *Chem. Soc. Rev.* **2019**, *48*, 2518–2534.
- [40] Y. He, W. J. Jiang, Y. Zhang, L. B. Huang, J. S. Hu, *J. Mater. Chem. A* **2019**, *7*, 18428–18433.
- [41] J. Wu, S.-G. Sun, X.-D. Zhou, *Nano Energy* **2016**, *27*, 225–229.
- [42] B. De Mot, J. Hereijgers, M. Duarte, T. Breugelmans, *Chem. Eng. J.* **2019**, *378*, 1–8.
- [43] S. Park, D. T. Wijaya, J. Na, C. W. Lee, *Catalysts* **2021**, *11*, 1–30.
- [44] W. Luc, B. H. Ko, S. Kattel, S. Li, D. Su, J. G. Chen, F. Jiao, *J. Am. Chem. Soc.* **2019**, *141*, 9902–9909.
- [45] J. Y. Kim, D. Hong, J. C. Lee, H. G. Kim, S. Lee, S. Shin, B. Kim, H. Lee, M. Kim, J. Oh, G. Do Lee, D. H. Nam, Y. C. Joo, *Nat. Commun.* **2021**, *12*, 1–11.
- [46] R. W. G. Wyckoff, *Cryst. Struct.* **1963**, *1*, 7–83.
- [47] J. F. Moulder, W. F. Stickle, P. E. Sobol, K. D. Bomben, *Handbook of X-Ray Photoelectron Spectroscopy*, Perkin-Elmer Corporation, Eden Prairie, Minnesota, **1992**.
- [48] J. Fayos, *J. Solid State Chem.* **1999**, *148*, 278–285.
- [49] W. J. Moore, L. Pauling, *J. Am. Chem. Soc.* **1941**, *63*, 1392–1394.

Manuscript received: October 10, 2022

Revised manuscript received: January 5, 2023